RSC Advances

ROYAL SOCIETY OF CHEMISTRY

PAPER

View Article Online
View Journal | View Issue

Check for updates

Cite this: *RSC Adv.*, 2023, **13**, 17370

Influence of ZIF-9 and ZIF-12 structure on the formation of a series of new Co/N-doped porous carbon composites as anode electrodes for high-performance lithium-ion batteries†

Anh T. A. Duong,[a] Hoang V. Nguyen,[bc] Man V. Tran,[bc] Quynh N. Ngo,[a] Loc C. Luu,[d] Tan L. H. Doan,[ef] Hung N. Nguyen[a] and My V. Nguyen*[a]

Received 28th April 2023
Accepted 31st May 2023

DOI: 10.1039/d3ra02802j

rsc.li/rsc-advances

A series of new Co/N-doped porous carbon composites, denoted as Co/CZIF-9 and Co/CZIF-12, containing Co nanoparticles encapsulated in nitrogen-doped carbon matrices were prepared by annealing Co-based zeolite imidazolate framework materials, ZIF-9 and ZIF-12, as the efficient precursors at different temperatures. The structural features of the as-synthesized composites at 900 °C were determined by analytical methods with high reliability. Consequently, Co/CZIF-12_900 exhibits a high first specific discharge capacity of 971.0 mA h g^{-1} at a current density of 0.1 A g^{-1}. Notably, the specific discharge/charge capacity of Co/CZIF-12_900 reaches about 508.8 mA h g^{-1} at 0.1 A g^{-1} after 100 cycles. The outstanding behaviors can be accounted for by the efficient incorporation of hetero-nitrogen doping and the Co nanoparticles within the layered structure of porous carbon, enhancing electrical conductivity and structural stability and limiting volume change during the intercalation/deintercalation of Li$^+$ ions. These findings suggest that the Co/CZIF-12_900 material could be employed as a promising anode electrode for energy storage products.

1. Introduction

Owing to the increasing demand for energy use with various targets, investigations seeking devices for energy conversion and storage have attracted much attention from scientists.[1–4] Recently, lithium-ion batteries (LIBs) have emerged as an excellent energy-storage device and are utilized in electronic products such as laptops, smartphones, portable devices, and hybrid vehicles.[5–8] However, there are requirements to improve the more effective electrochemical properties of LIBs for real-file applications.[9,10] It is necessary to find new LIBs capable of operating in practical conditions with high energy density and storage capacity. Graphite is considered a commercial anode material for LIBs, but its low theoretical capacity of 372 mA h g^{-1} has urged studies towards other alternative anode materials.[11–13] Fortunately, porous carbon materials possess the unique features to cope with the mentioned drawbacks, such as volumetric strain decrease, rapid ionic diffusion, and high electrical conductivity.[14–16] Besides, heteroatom doping and pore distribution within porous carbon play a vital role in electrochemical properties.[17,18] Hence, the incorporation of porous frameworks and heteroatom doping into nanoporous carbon is recognized as a potential approach for effective energy storage.

The fact shows that the distribution of metal moieties into the carbon matrix could significantly improve the mechanical performance and conductivity, enhancing the cycling and rate property of porous carbon material. In general, the weak interactions between the carbon backbone and metal compounds cause the loss of Li$^+$ storage capacity under long-term cycling and high current density. Therefore, there are challenges to designing novel LIB systems containing strong attractions between the metal sites and porous carbon framework.

Metal–organic frameworks (MOFs), as a generation of porous materials, have attracted many investigations due to their extraordinary factors such as facile fabrication, high thermal and chemical robustness, low density, and high ordered structure.[19–21] MOFs are constructed from the metal

---

[a] Faculty of Chemistry, Ho Chi Minh City University of Education, Ho Chi Minh City 700000, Vietnam. E-mail: mynv@hcmue.edu.vn

[b] Applied Physical Chemistry Laboratory (APCLAB), VNUHCM-University of Science, Ho Chi Minh City 700000, Vietnam

[c] Department of Physical Chemistry, Faculty of Chemistry, VNUHCM-University of Science, Ho Chi Minh City 700000, Vietnam

[d] HCMC University of Technology, VNU-HCM, 268 Ly Thuong Kiet, District 10, Ho Chi Minh City, Vietnam

[e] Center for Innovative Materials and Architectures (INOMAR), Ho Chi Minh City, Vietnam

[f] Vietnam National University, Ho Chi Minh City, Vietnam

† Electronic supplementary information (ESI) available: Full characterization and electrochemical measurement details. See DOI: https://doi.org/10.1039/d3ra02802j

clusters and organic ligands, forming three-dimensional frameworks containing the various crystalline structures with adjusted pore diameters and functional groups onto the organic linkers. Thus, MOF materials indicate the dominant achievements in gas storage,[22] environmental treatment,[23–26] catalysis,[27,28] sensing,[29,30] and energy conversion.[31–33] Noteworthily, cobalt-based zeolite imidazolate framework (Co-ZIF) is a typical Co-based MOFs material employed as an outstanding precursor for the generation of Co/nitrogen-doped (N-doped) nanoporous carbon as an anode material for enhancing the electrochemical behaviors of LIBs. For instance, Z. Li *et al.* prepared CoSe/NC composites derived from ZIF-67 exhibiting a reversible capacity of 310.1 mA h g^{-1} after 500 cycles at 1.0 A g^{-1}.[34] Y. Chang *et al.* used Co/ZnO/N-doped ZIF-8 and ZIF-67-derived carbon as an efficient anode material for LIBs with a capacity of 411.0 mA h g^{-1} at 0.2 A g^{-1} after 100 cycles.[35] It is noted that the presence and strong interaction of N heteroatom doping and the reduced Co nanoparticles within N-doped porous carbon materials after the carbonization process of initial ZIF precursors can prevent volume expansion and facilitate improving storage capacity, ionic conductivity, cycling stability, and catalytic activity of graphitization process.[36,37] Nevertheless, almost the previous reports are only based on the reagents derived from the family of ZIF-67 and ZIF-8 materials and have yet to elucidate the effect of ZIF structure on the formation of different N-doped porous carbons for improving the electrochemical performance in LIBs. Inspired by this, we expect that ZIF-9 and ZIF-12 materials with different structures fabricated from the similarly initial precursors, including Co^{2+} salt and benzimidazole linker at room temperature, are promising anode electrodes after carbonization for considerable improving the Li$^+$ storage capacity. This is a new approach to demonstrate the influence of Co-ZIF structure on the difference of the Li-ion reversible capacity and deal with the stated disadvantages during the operating process of LIBs.

With all of this considered, we propose a research strategy using two Co/N-doped porous carbon materials prepared from the various SOD-type and RHO-type ZIF structures, denoted as Co/CZIF-9 and Co/CZIF-12, as effective anode electrodes for high-performance LIBs. Full characterizations of Co/CZIF-9 and Co/CZIF-12 materials were confirmed by the combined methods such as Fourier transform infrared spectroscopy (FT-IR), Raman spectroscopy, the thermogravimetric analysis combined with differential scanning calorimetry (TGA-DSC), scanning electron microscopy (SEM), energy-dispersive X-ray mapping (EDX-mapping), and transmission electron microscopy (TEM), Brunauer–Emmett–Teller (BET), and X-ray photoelectron spectroscopy (XPS). In particular, Co/CZIF-12_900 annealed at 900 °C possesses a high reversible capacity of 508.8 mA h g^{-1} after 100 cycles at 0.1 A g^{-1}, which is higher than the capacity of Co/CZIF-9_900 (367.5 mA h g^{-1}) in the same measurement condition. Furthermore, the reversible capacity of Co/CZIF-12_900 reaches a value of 309.2 mA h g^{-1} at a high current density of 1 A g^{-1}. The obtained data prove that Co/CZIF-12_900 is a potential candidate as an efficient anode electrode for enhancing the LIB performance.

2. Experimental section

2.1 Materials and procedures

Cobalt acetate tetrahydrate ($Co(Ac)_2 \cdot 4H_2O$, 98%), benzimidazole (Bim, 98%), ammonium hydroxide (30%), ethanol (EtOH, 99%), methanol (MeOH, 99%), toluene (99%), and acetone (99%) were purchased from commercially available sources and used without further purification. Water used was double distilled and filtered through a Millipore membrane.

Thermogravimetric analysis (TGA) and differential scanning calorimetry (DSC) curves were carried out on a thermal analysis system (Labsys Evo 1600 TGA, SETARAM) under dry airflow and N_2 medium in the temperature range of 25–1000 °C at a rate of 5 °C min^{-1}. Fourier transform infrared (FT-IR) spectra were conducted on a spectrometer with the Attenuated Total Reflectance (ATR) sampling method (Vertex 70, Bruker). Raman spectroscopy analysis was performed on a spectrometer (XploRA one 532 nm, Horiba). Low-pressure N_2 adsorption analyses were carried out on a surface characterization analyzer (TriStar II Plus, Micromeritics). A liquid N_2 bath was used for measurements at 77 K. Before N_2 sorption measurements, and the materials were activated at 150 °C under vacuum for 24 h. Powder X-ray data were analyzed on a diffractometer (D8 Advance, Bruker) using Ni filtered Cu Kα (λ = 1.54718 Å). Scanning electron microscopy (SEM) images were collected on a microscope (FESEM S-4800, Hitachi) with an accelerating voltage of 10 kV. Energy-dispersive X-ray (EDX) analysis was conducted on an instrument (EDX H-7593, Horiba). Transmission electron microscopy (TEM) was performed on a microscope (Jeon 1010, Hitachi) with a high voltage of 80 kV. X-ray photoelectron spectroscopy (XPS) was conducted using an X-ray photoelectron spectrometer (PHI 5000, Chigasaki) equipped with a monochromatic Al Kα source operating at 50 W and 15 kV.

2.2 Synthesis of ZIF-9

According to previous reports,[38,39] a mixture of $Co(Ac)_2 \cdot 4H_2O$ (125 mg, 0.502 mmol) and Bim (120 mg, 1.017 mmol) was introduced to a 50 mL glass bottle containing 0.26 mL of ammonium hydroxide and 8.75 mL of EtOH solvent. The mixture was stirred with a constant rate at room temperature for 4 h. Then, the mixture was centrifuged to acquire a purple solid. The product was washed with EtOH for 48 h (40 mL per day) to detach unreacted substances and exchanged with acetone for 48 h (40 mL per day). Finally, the sample was centrifuged, dried, and activated under vacuum at 80 °C for 24 h to yield a pure sample, termed ZIF-9.

2.3 Synthesis of ZIF-12

According to previous reports,[38,39] a mixture of $Co(Ac)_2 \cdot 4H_2O$ (125 mg, 0.502 mmol) and Bim (120 mg, 1.017 mmol) was added to a 50 mL glass bottle including 0.27 mL of ammonium hydroxide, 6.10 mL of MeOH and 5.31 mL of toluene solvent. The mixture was stirred with a constant rate at room temperature for 4 h. Then, the mixture was centrifuged to obtain a purple solid. The solid was washed with MeOH for 48 h (40 mL per day) to remove unreacted substances and exchanged with acetone for 48 h (40 mL per day). Subsequently, the product was centrifuged, dried, and activated under vacuum at 80 °C for 24 h to yield a pure solid, namely ZIF-12.

2.4 Fabrication of Co/CZIF-9

100 mg of ZIF-9 was annealed at 700, 800, 900 °C for 4 h in an N_2 atmosphere to obtain three Co/N-doped porous carbon derived from ZIF-9. These materials were then washed with distilled water, EtOH, and dried under vacuum at 80 °C for 24 h. For convenience, these materials are abbreviated as Co/CZIF-9_700, Co/CZIF-9_800, and Co/CZIF-9_900, respectively.

2.5 Fabrication of Co/CZIF-12

100 mg of ZIF-12 was calcined at 700, 800, 900 °C for 4 h in an N_2 medium to yield three Co/N-doped porous carbon derived from ZIF-12. These composites were then washed with distilled water, EtOH, and dried under vacuum at 80 °C for 24 h. For convenience, these composites are abbreviated as Co/CZIF-12_700, Co/CZIF-12_800, and Co/CZIF-12_900, respectively.

2.6 Electrochemical studies

The electrode was prepared by mixing the Co/N-doped porous carbon (80%), conductive carbon super P (15%), and polyvinylidene fluoride (PVdF) (5%) as a binder into an appropriate amount of *N*-methyl pyrrolidone (NMP) on a Thinky mixer at 2000 rpm for 20 min then coated on a Cu foil, dried at 110 °C for 12 h in a vacuum and subsequently punched into disks (13 mm in diameters). The active mass loading of the electrode was 2–3 mg cm^{-2}.

The as-prepared electrode was then assembled in coin cell CR2032 in an Ar-filled glovebox, with a lithium foil as the counter and reference electrode, Celgard 2400 as a separator, and the electrolyte was 1 M $LiPF_6$ in ethylene carbonate (EC)/diethyl carbonate (DEC) (1 : 1 by volume). The water and O_2 concentration of the glovebox were controlled below 0.1 ppm. A Lanhe CT3001A battery tester was used to perform the electrochemical measurement on the coin cell. The scanning rate used in the cyclic voltammetry (CV) test was 0.1 mV s^{-1}. The charge/discharge test was carried out within the voltage of 0.01–3 V, and the current density was 0.1 A g^{-1}. Meanwhile, the rate capability was conducted within the same voltage, using the increase of current density from 0.1 to 5 A g^{-1}. The

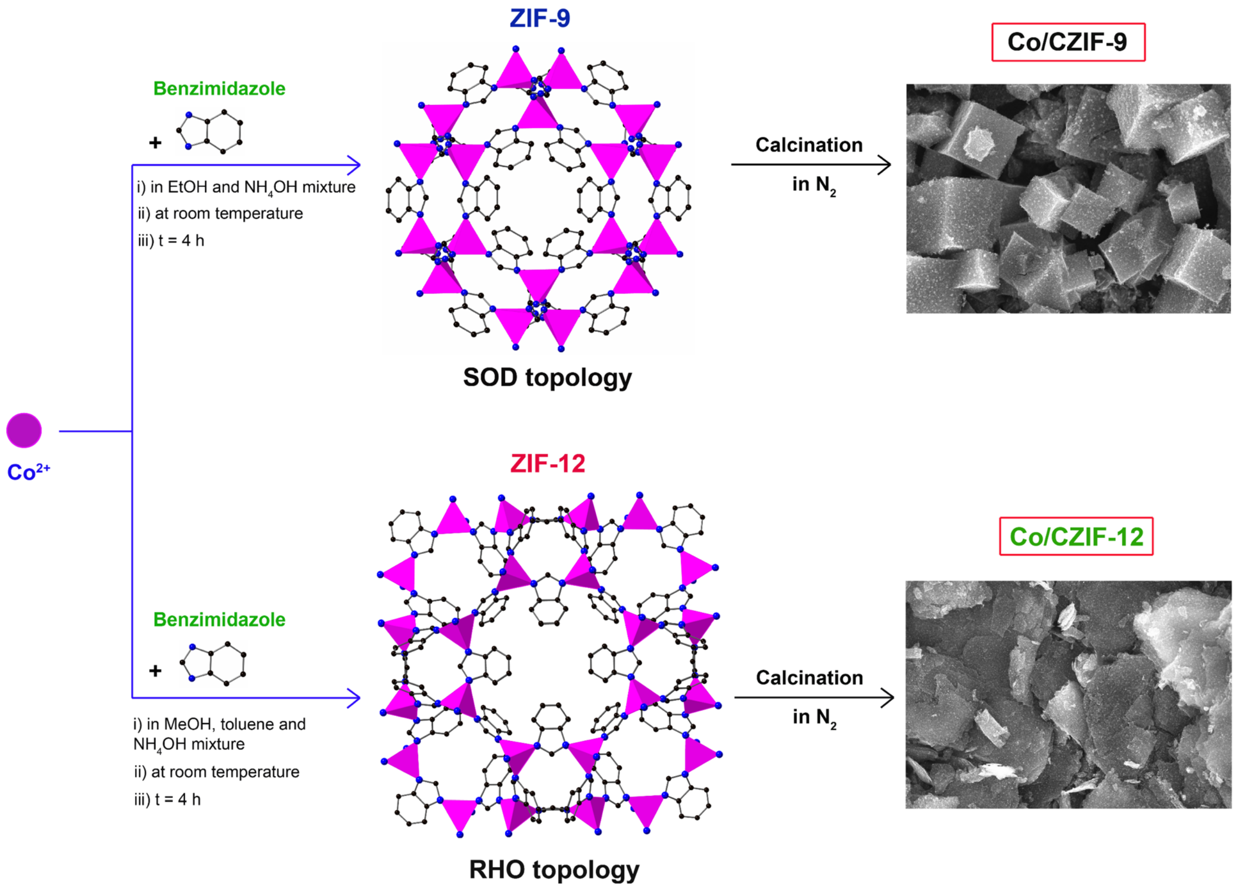

Fig. 1 The structure of ZIF-9 and ZIF-12 backbone is constructed from the Co tetrahedral and benzimidazole linkers, indicating the different topologies and the SEM images of Co/N-doped porous carbon, denoted as Co/CZIF-9 and Co/CZIF-12 derived from the ZIF-9 and ZIF-12 precursors. The architectures of ZIF-9 and ZIF-12 are depicted from the cif information with the CCDC numbers 1036076 and 602546, respectively. Atom colors: Co, pink polyhedra; C, black; N, blue. All H atoms are omitted for clarity.

electrochemical impedance spectroscopy (EIS) was performed on a VSP3 (Biologic) instrument with a frequency range of 10^6 and 10^{-2} Hz and a perturbation amplitude of 10 mV.

3. Results and discussion

3.1 Synthesis and characterization of ZIF and Co/N-doped porous carbon materials

To prove the influence of ZIF structure on the generation of various Co/N-doped porous carbon composites for improving the LIB performance, we fabricated two Co-based ZIF precursors with different topologies, denoted as ZIF-9 and ZIF-12, constructed from the CoN_4 tetrahedral units and benzimidazole (Bim) ligands (Fig. 1). Accordingly, ZIF-9 was prepared by blending the Bim linker and Co^{2+} salt in EtOH solvent with a presence of ammonium hydroxide as a modulator for the crystal nucleation.[38,39] Herein, ZIF-9 crystallizes in the hexagonal symmetry with a SOD topology containing two Co ions linked by each Bim linker. Noteworthily, ZIF-9 possesses a pore diameter of 2.9 × 4.3 Å. Meanwhile, ZIF-12 was synthesized by mixing the Co^{2+} ions and Bim linker with a similar modulator of ammonium hydroxide in another solvent mixture, including MeOH and toluene, leading to the generation of another structure as compared to the ZIF-9 structure. In detail, ZIF-12 contains the Co tetrahedral unit bridged with four nitrogen atoms of Bim linker to create an extended three-dimensional system with an RHO topology.[38,39] Compared with ZIF-9, ZIF-12 adopts larger cages with a pore diameter of 3.0 × 14.6 Å. With this feature, ZIF-12 was a promising candidate for the previous works.[40,41] With the appearance of Co metal sites and N atoms inside the obtained ZIF structures, we hope that the carbonization process of these materials will create a series of new Co/N-doped nanoporous carbon composites capable of the significant enhancement of electrochemical performance in LIBs. Consequently, ZIF-9 and ZIF-12 were annealed at different temperatures, such as 700, 800, and 900 °C, under an N_2 atmosphere to form the new composites, namely Co/CZIF-9 and Co/CZIF-12, respectively.

The phase purity of ZIF and Co/CZIF materials was evaluated by powder X-ray diffraction (PXRD) analyses, in which the PXRD patterns of the pristine ZIF-9 and ZIF-12 samples were in good agreement with the previous literature (Fig. 2a).[38,39] Fig. 2a–c exhibit the PXRD diagrams of Co/CZIF-9 and Co/CZIF-12 calcined at 700, 800, and 900 °C. The peaks at (111), (200), (220) planes are in good accordance with the standard diagram of the Co particles. When the annealing temperature is raised, the diffraction peaks tend to be sharper and narrower, showing the rise in particle size. Also, the sharpness of the (111) plane is more apparent than the remaining peaks, indicating a dominant crystal growth at the (111) peak,[42] and has the highest intensity at 900 °C for both Co/CZIF-9 and Co/CZIF-12. It is noted that the structure of composites becomes more stable at

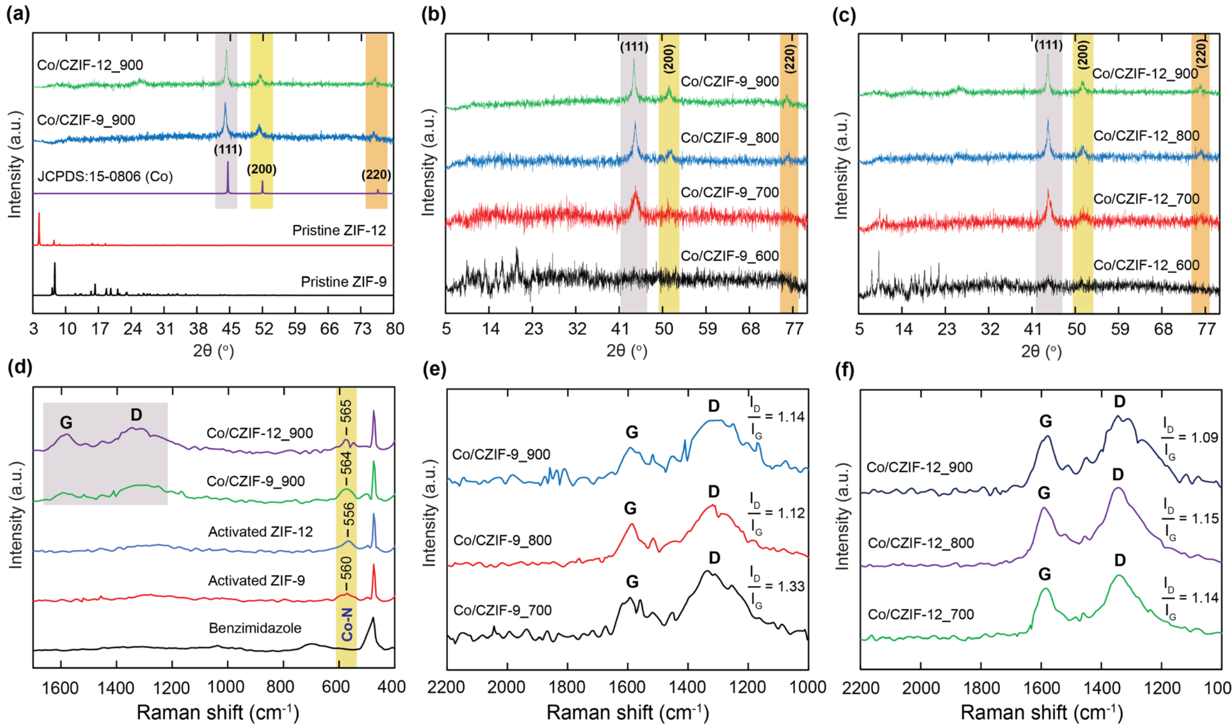

Fig. 2 PXRD patterns of the pristine ZIF-9 (black), pristine ZIF-12 (red), Co/CZIF-9_900 (blue), and Co/CZIF-12_900 (green) in comparison with Co nanoparticles (purple) (a); PXRD analyses of Co/CZIF-9_600 (black), Co/CZIF-9_700 (red), Co/CZIF-9_800 (blue), and Co/CZIF-9_900 (green) samples (b); PXRD patterns of Co/CZIF-12_600 (black), Co/CZIF-12_700 (red), Co/CZIF-12_800 (blue), and Co/CZIF-12_900 (green) samples (c); Raman spectra of the activated ZIF-9 (red), activated ZIF-12 (blue), Co/CZIF-9_900 (green), and Co/CZIF-12_900 (purple) as compared to the benzimidazole linker (black) (d); Raman spectra of the Co/CZIF-9_700 (black), Co/CZIF-9_800 (red), and Co/CZIF-9_900 (blue) (e); Raman spectra of the Co/CZIF-12_700 (green), Co/CZIF-12_800 (purple), and Co/CZIF-12_900 (dark blue) (f).

a higher temperature, resulting in the Li^+ convenient storage and diffusion.[43] Notably, the PXRD patterns of Co/CZIF-9_600 and Co/CZIF-12_600 display the absence of Co nanoparticle peaks. This can be attributed to the fact that the structure of ZIF-9 and ZIF-12 still contains the metal clusters and organic ligand moieties and not completely decomposes to generate the perfect Co/N-doped nanoporous carbon at 600 °C, causing the difference of these PXRD diagrams in comparison with the PXRD patterns at 700, 800, and 900 °C. Hence, we choose the ZIF samples after annealing 700, 800, and 900 °C as the anode electrodes for measuring the electrochemical properties in LIBs. Next, Raman spectra of ZIF and Co/CZIF samples reveal the presence of two broad bands, D- and G-bands, at 1335 and 1580 cm^{-1}, respectively (Fig. 2d–f). These vibrations illustrate the defects and ordered graphitic carbon of carbon materials within Co/N-doped nanoporous carbon. The ratios of I_D/I_G are in the range from 1.09 to 1.33, showing a low graphitization level of the composites, and there are defects with the increase of calcination temperature.[36,44–46] Herein, the defects in carbon materials can support the Li^+ facile diffusion process, leading to the enhancement of storage capacity.

Interestingly, the signals are exposed at 560 and 556 cm^{-1}, relating to the characteristic vibrations of Co–N, which are present in the ZIF-9 and ZIF-12 spectra, respectively. Moreover, the Co–N bands are also found at 564 and 565 cm^{-1} in Co/CZIF-9_900 and Co/CZIF-12_900 spectra, respectively. Herein, the appearance of the Co–N bond within Co/CZIF-9 and Co/CZIF-12 composites exhibits the interaction between the Co nanoparticles and N-doped porous carbon backbone as a chemical attraction, driving the improvement of active electrical connections between the N-doped porous carbon and Co atoms, in addition, minimizes the volume change of these composites.[34] Furthermore, the FT-IR spectra of all samples were conducted and clearly illustrated in Section S1.† Consequently, Fig. S1 and S2† indicate the presence of C═N, C═C, imidazole ring, and Co–N bands within all materials, appearing at 1521–1524 cm^{-1}, 1457–1490 cm^{-1}, 1033–1049 cm^{-1}, and 526–550 cm^{-1}, respectively. Whereas the appearance of C–H vibrations inside the ZIF-9 and ZIF-12 materials is confirmed by the signals located at 735–736 cm^{-1} and 1270–1272 cm^{-1}, but absent in the Co/CZIF-9 and Co/CZIF-12 spectra. This is reasonable because these composites no longer contain the C–H characteristic bands after carbonization.

To select the suitable calcination temperature for forming Co/N-doped composites, the TGA-DSC analyses of ZIF-9 and ZIF-12 were carried out under N_2 and dry air (80% N_2, 20% O_2)

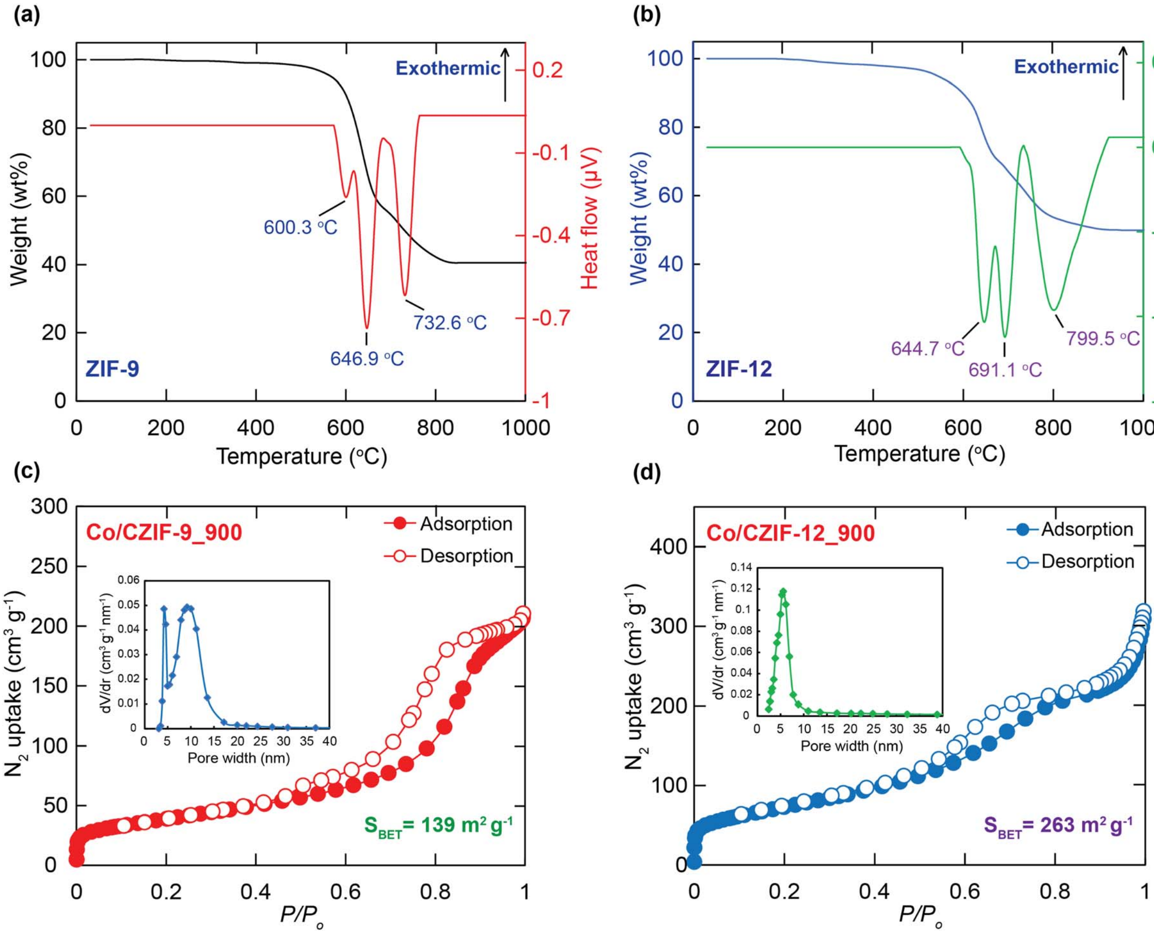

Fig. 3 TGA-DSC curve of the activated ZIF-9 material under an N_2 atmosphere (a); TGA-DSC diagram of the activated ZIF-12 sample under an N_2 medium (b); N_2 adsorption–desorption isotherm and pore size distribution of Co/CZIF-9_900 (c); N_2 adsorption–desorption isotherm and pore size distribution of Co/CZIF-12_900 (d).

medium, as revealed in Fig. 3a, b and Section S2.† Accordingly, the frameworks of ZIF-9 and ZIF-12 lost considerable weight at 500–700 °C and totally decomposed at 800 °C with specific endothermic and exothermal peaks. This situation is in good agreement with the mentioned PXRD analyses in this work. The residue percentages of Co/CZIF-9 and Co/CZIF-12 are 40.56 and 49.85 wt%, respectively (Fig. 3a and b). Hence, the optimal annealing temperatures of 700, 800, 900 °C are chosen to synthesize the composites for the subsequent electrochemical studies.

N_2 isotherm curves were performed to evaluate the porosity and pore size within the Co/N-doped materials. Fig. 3c and d display that the N_2 adsorption/desorption isotherms of Co/CZIF-9_900 and Co/CZIF-12_900 are typical type I and IV curves with the hysteresis loops in the range of relative pressure 0.5–0.9 P/P_0, containing combined microporous and mesoporous characterization within the structure. This proves that Co/CZIF-9_900 and Co/CZIF-12_900 possess a hierarchical porous structure. The N_2 uptake capacity of all composites tends the increase at higher calcination temperatures (Fig. S5†). Noteworthily, the BET (Langmuir) surface area of Co/CZIF-9_900 and Co/CZIF-12_900 materials reach the highest values of 139 (213) $m^2\ g^{-1}$ and 263 (411) $m^2\ g^{-1}$, respectively (Fig. 3c, d, S6, and S7†). The high surface area and mesoporous structure of Co/N-doped porous carbon materials can significantly enhance the Li^+ rapid diffusion and electrolyte penetration with low resistance and prevent volume expansion during the discharge/charge process.[34,43] Following these features, Co/CZIF-9_900 and CZIF-12_900 emerge the potential candidates as efficient anode electrodes for LIBs.

Furthermore, the XPS measurements reveal that the surface of Co/CZIF-9_900 and Co/CZIF-12_900 presents the C, N, O, Co elements (Fig. 4). Herein, the signals at 542.08 eV and 545.08 eV for Co/ZIF-9_900 and Co/CZIF-12_900, respectively, are attributed to the presence of O 1s component derived from the exposure of the samples in the air. In detail, the C 1s spectra indicate four peaks at 284.7 eV, 284.9 eV, 286.0 eV, and 289.6 eV for Co/CZIF-9_900 and Co/ZIF-12_900, corresponding to the C=C, C–C, C–N, and C=N, respectively.[43,47] This result is in good accordance with the obtained FT-IR and Raman spectra. Remarkably, the C–N and C=N bonds prove the possible existence of N atoms within the carbon matrix of Co/N-doped porous carbon. The N 1s spectra can be deconvoluted into the peaks at 398.8 eV, 401.5 eV, and 402.0 eV/402.9 eV, which are accounted for the formation of pyridinic N, pyrrolic N, and graphitic N types, respectively, suggesting that Bim linker was transferred to the Co/N-doped porous carbon *via* the annealing.[36,48] These N-doped moieties can effectively connect to the C atoms inside Co/CZIF-9_900 and Co/CZIF-12_900, resulting in the remarkable improvement of the ionic conductivity and Li^+ storage capacity. Furthermore, the Co 2p spectra of these composites are deconvoluted into six characteristic peaks, termed CoO_x (778.5 eV), Co $2p_{3/2}$ (780.3 eV), Co^{2+} satellites (783 eV/782.6 eV), CoO_x (789.2 eV/788.9 eV), Co $2p_{1/2}$ (795.7 eV/795.5 eV), Co^{2+} satellites (802.4 eV/802.1 eV).[49,50] As given in Fig. 5, the SEM image shows that Co/CZIF-9_900 still retains the morphology of the ZIF-9 nanocubes. Nevertheless, the surface of Co/CZIF-9_900 is rougher than ZIF-9. This can be attributed to the decay process of the original ZIF-9 precursor. The particle sizes of the ZIF-9 and Co/CZIF-9_900 samples are about 1–2 μm. Meanwhile, the morphology of Co/CZIF-12_900 possesses the form of stacked carbon layers, which are completely different from the rhombic dodecahedral shape of ZIF-12. It is explained that the volume expansion and collapse of the ZIF-12 structure after calcination cause significant changes in the morphology. This phenomenon is also observed in the reported literature.[34]

Owing to the layered structural feature, Co/CZIF-12_900 is similar to the commercial graphite morphology, driving many promising commercial applications for this material with excellent electrochemical properties. The TEM images of the ZIF and composites indicate that the Co dark points with various sizes of 10–50 nm asynchronously locates within the porous carbon matrix (Fig. S8†). Besides, the EDX-mapping spectra of the materials are conducted and shown in Fig. 6, S9, and S10.† Consequently, the uniform distribution of C, N, and Co elements within the ZIF and composites further demonstrates the reliable existence of Co and N in the initial ZIF precursors and Co/N-doped porous carbon materials. All of the evidence mentioned above, gained from PXRD, Raman, FT-IR, TGA-DSC, BET, XPS, SEM, TEM, and EDS analyses, confirm that the Co/N-doped nanoporous carbon materials have been successfully fabricated after annealing at high temperatures.

3.2 Electrochemical measurements of the Co/CZIF-9 and Co/CZF-12 materials

To understand the electrochemical possibilities of these Co/N-doped porous carbon materials, we used the composites such as Co/CZIF-9_700, Co/CZIF-9_800, Co/CZIF-9_900, Co/CZIF-12_700, Co/CZIF-12_800, and Co/CZIF-12_900 as the anode electrode materials for systematical analyzing the electrochemical performances of cyclic voltammetry (CV), galvanostatic discharge/charge voltage test, cycling and rate performance, and electrochemical impedance spectroscopy (EIS) in a coin-type half-cell. The preliminary results show that the samples calcined at 900 °C, termed Co/CZIF-9_900 and Co/CZIF-12_900, exhibit the dominant Li^+ storage capacity after 100 cycles. This property is consistent with the perfect structure of these composites, as evidenced in the above complete characterizations. Thus, Co/CZIF-9_900 and Co/CZIF-12_900 are chosen for further discussion about the subsequent electrochemical experiments in this main paper. Additionally, as a full comparison and consideration of the effect of the structure on the electrochemical performance, the electrochemical studies for the remaining Co/N-doped nanoporous carbon materials (annealed at 700 and 800 °C) are clearly illustrated in Section S5.†

The CV curves of the Co/CZIF-9_900 and Co/CZIF-12_900 for the initial three cycles in the potential range of 0.01–3.0 V at a scan rate of 0.1 mV s^{-1} are indicated in Fig. 7a and c. During the initial cathodic sweep, there are two strong reduction peaks at 0.56 V and 1.73 V for Co/CZIF-9_900 and 0.73 V and 1.71 V for Co/CZIF-12_900, which are ascribed to the electrolyte degradation and the generation of the solid electrolyte interface (SEI)

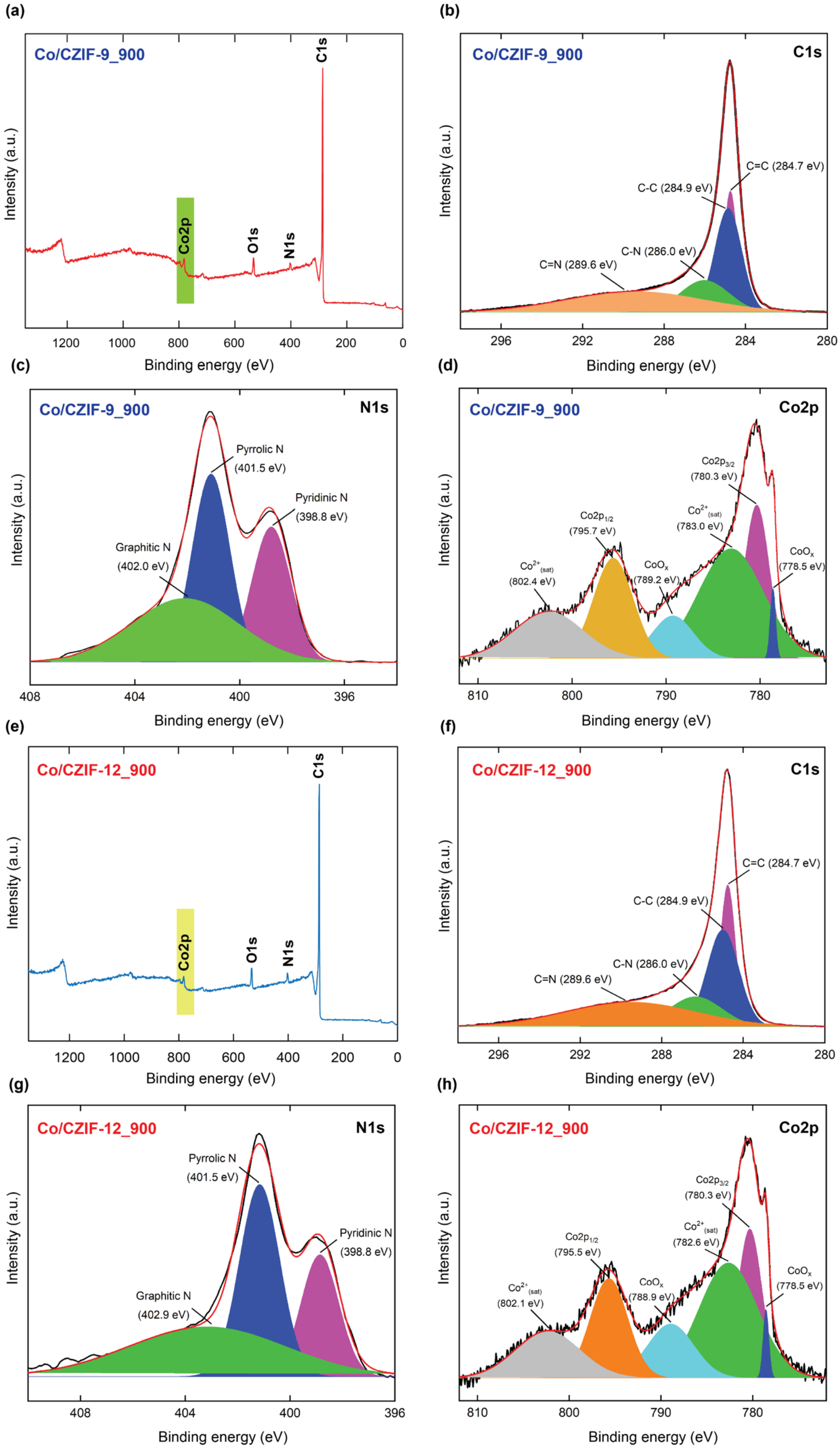

Fig. 4 XPS spectra of the Co/CZIF-9_900 and Co/CZIF-12_900: the survey of Co/CZIF-9_900 (a); C 1s of Co/CZIF-9_900 (b); N 1s of Co/CZIF-9_900 (c); Co 2p of Co/CZIF-9_900 (d); the survey of Co/CZIF-12_900 (e); C 1s of Co/CZIF-12_900 (f); N 1s of Co/CZIF-12_900 (g); Co 2p of Co/CZIF-12_900 (h).

layer.[51–53] These peaks vanished in the following cycles indicating the formation of a subsequent stable SEI layer preventing the reduction process of the electrochemically driven electrolyte. In the consecutive cathodic scans, the reduction peaks shift to a new high potential position of 1.05 V for Co/CZIF-9_900 and 1.04 V for Co/CZIF-12_900 and low potential

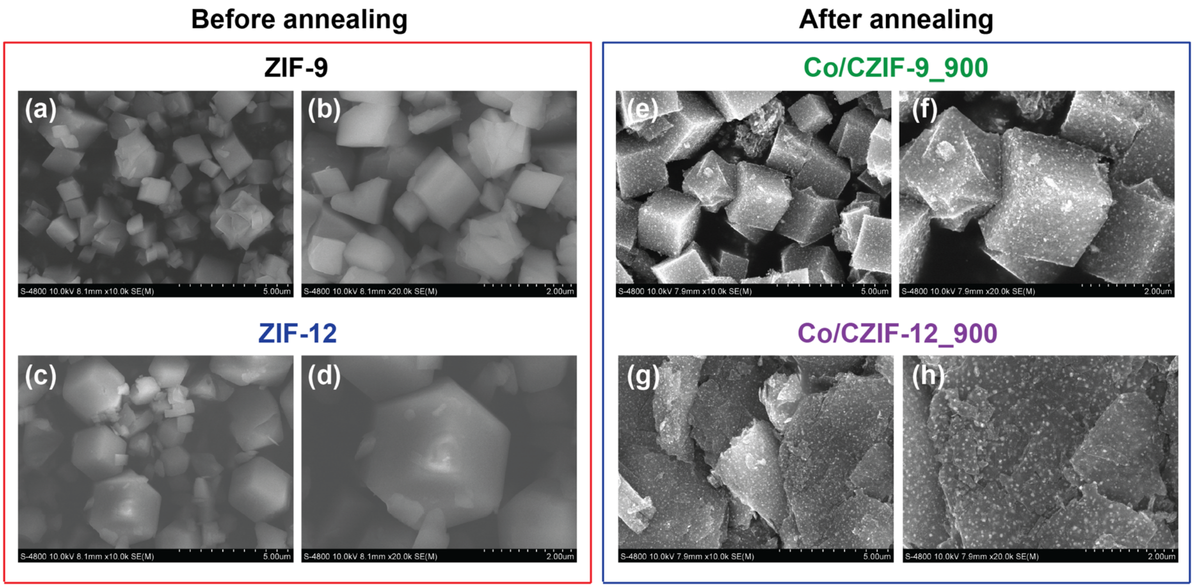

Fig. 5 SEM images of the ZIF-9 material (a and b); ZIF-12 material (c and d); Co/CZIF-9_900 composite annealed at 900 °C (e and f); and Co/CZIF-12_900 composite calcined at 900 °C (g and h).

position closed to 0 V, relating to the intercalation of the Li^+ ions from the porous structure of the surface and into the carbon matrix, respectively.[54,55] The inversed process resulted in the peaks at 0.11 V and 1.04 V for Co/CZIF-9_900, 0.11 V, and 1.09 V for Co/CZIF-12_900 in the following anodic scan. Additionally, all consecutive scans are well overlapped compared to the initial sweep, indicating the outstanding reversibility and cycling stability of Co/CZIF-9_900 and Co/CZIF-12_900. It is

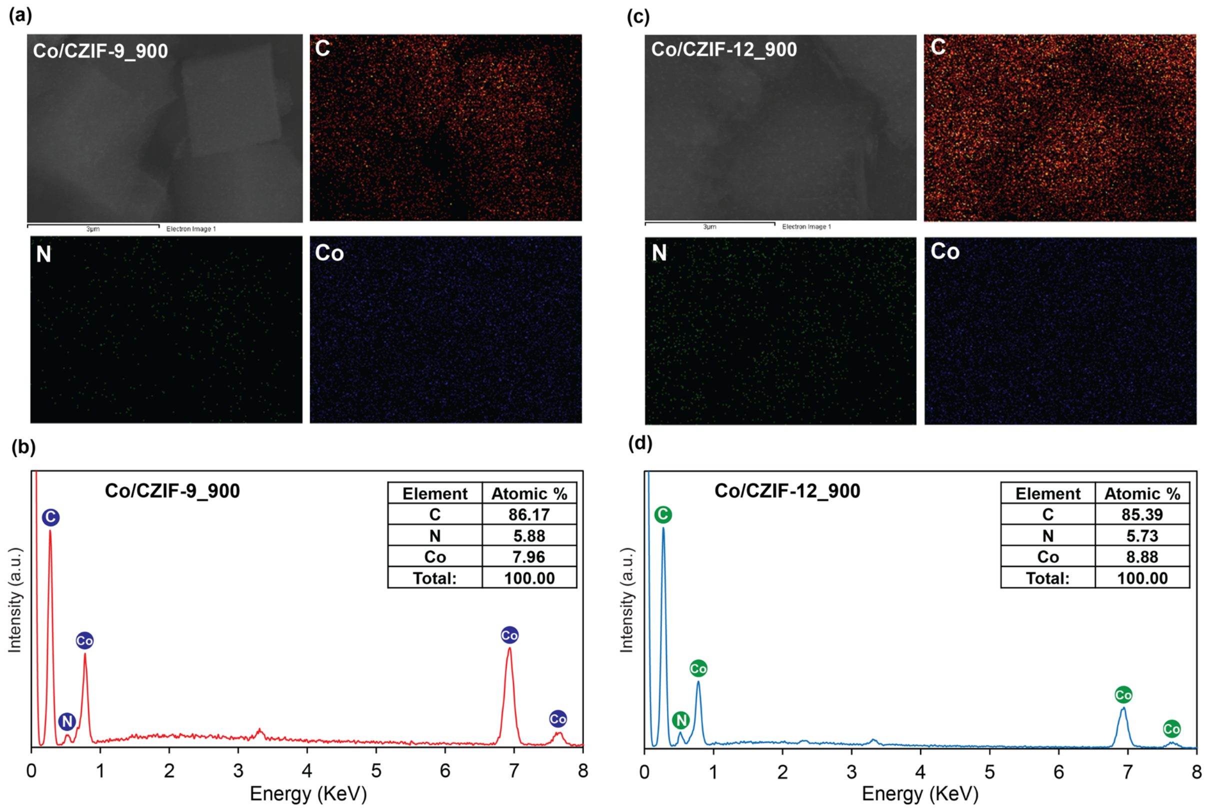

Element	Atomic %
C	86.17
N	5.88
Co	7.96
Total:	100.00

Element	Atomic %
C	85.39
N	5.73
Co	8.88
Total:	100.00

Fig. 6 Elemental mapping images of Co/CZIF-9_900 composites (a); EDS analysis of Co/CZIF-9_900 composite (b); elemental mapping images of Co/CZIF-12_900 composites (c); EDS analysis of Co/CZIF-12_900 composite (d).

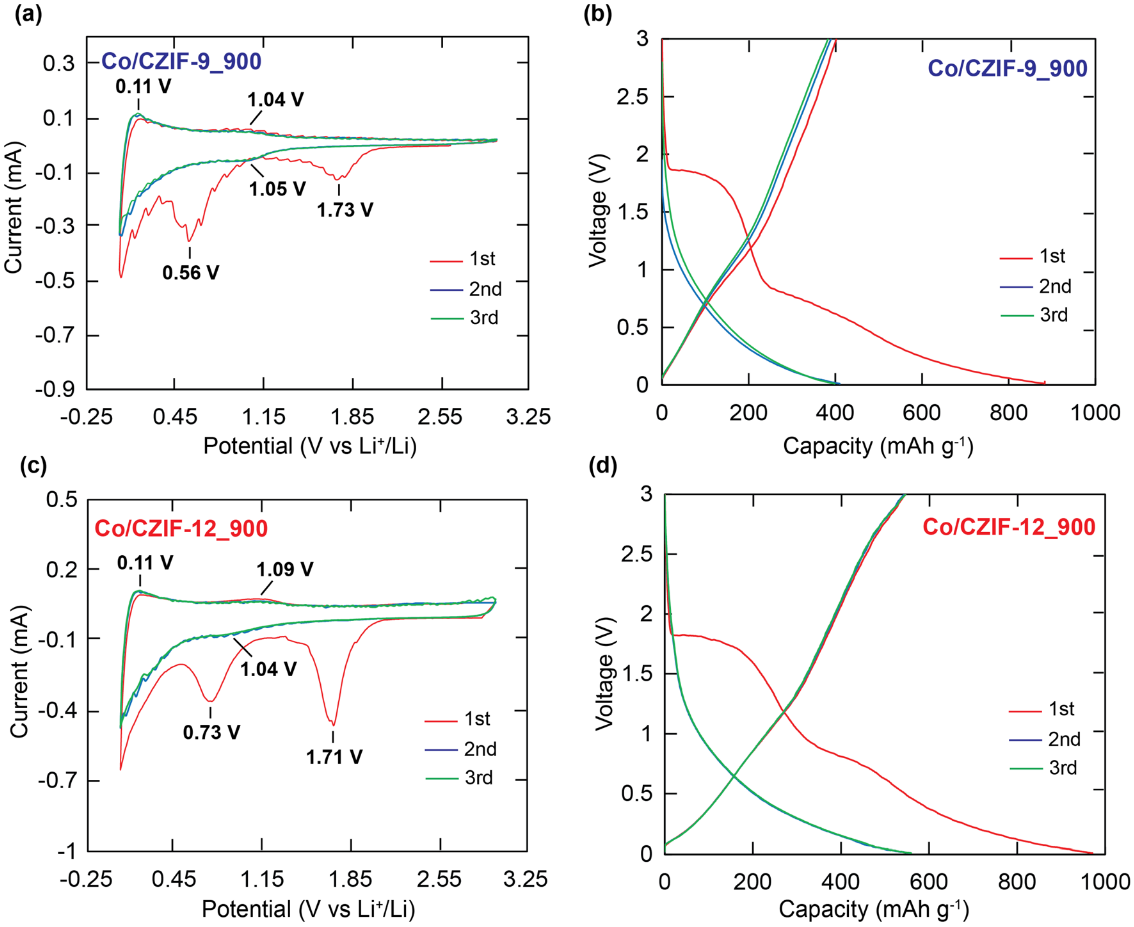

Fig. 7 The first three CV curves of Co/CZIF-9_900 at 0.1 mV s^{-1} in the potential range of 0.01–3.0 V (a); the discharge/charge curves of Co/CZIF-9_900 at a current density of 0.1 A g^{-1} for the first three cycles (b); the first three CV curves of Co/CZIF-12_900 at 0.1 mV s^{-1} in the potential range of 0.01–3.0 V (c); the discharge/charge curves of Co/CZIF-12_900 at a current density of 0.1 A g^{-1} for the first three cycles (d).

realized that the reduction and oxidation peaks of the electrochemical reaction between the Li$^+$ ions and the Co nanoparticles are not found during the positive and negative sweeps, as compared to the electrochemical reaction of cobalt-based composites reported previously.[43,56] These studies prove that even though the Co metal moieties support nothing to the Li$^+$ storage capacity, the introduced Co nanoparticles play a vital role in the improvement of the synergistic effect between the matrix carbon and Co particles, resulting in enhancing the electronic conductivity and structural robustness of the Co/N-doped porous carbon. Also, the CV curves of the remaining composites are entirely revealed in Section S5.†

Fig. 7b and d exhibit the galvanostatic discharge/charge profiles of Co/CZIF-9_900 and Co/CZIF-12_900 at a current density of 0.1 A g^{-1} in the initial three cycles. In the 1st discharge, the ranges of extended stable voltage for both materials are found at 1.79 V and 0.75 V, which are in good agreement with the position of the reduction peak in the mentioned CV data. The initial discharge capacities of Co/CZIF-9_900 and Co/CZIF-12_900 reach up to 883.1 and 971.0 mA h g^{-1}, relating to the initial coulombic efficiency of 45.60% and 56.30%, respectively. The decline of initial capacities is attributed to the formation of the SEI layer, and the other side reactions occurred.[43,57,58] Fortunately, the discharge/charge curves for subsequent cycles show no significant differences about 383.2 mA h g^{-1} for Co/CZIF-9_900 and 547.2 mA h g^{-1} for Co/CZIF-12_900, which demonstrate excellent cyclic robustness of these composites. Noteworthily, the specific discharge/charge capacities of Co/CZIF-9_900 and Co/CZIF-12_900 obtain about 367.5 and 508.8 mA h g^{-1} after 100 cycles at a current density of 0.1 A g^{-1} (Fig. 8a and b). The coulombic efficiencies of the materials after 100 cycles are 98.2% for Co/CZIF-9_900 and 99.5% for Co/CZIF-12_900. Herein, the anode electrodes prepared from the Co/CZIF porous carbon reveal durable long-life cyclic property at a current density of 0.1 A g^{-1}. Besides, the specific discharge capacities of Co/CZIF-9_700, Co/CZIF-9_800, Co/CZIF-12_700, and Co/CZIF-12_800 after 100 cycles are 208.1, 308.2, 377.63, and 408.6 mA h g^{-1}, respectively (Section S5†). It is noted that the specific capacities tend the increase with the calcination temperatures raised. Moreover, the specific discharge/charge capacity values of Co/CZIF-12 are much higher than Co/CZIF-9 composite, showing that the unique layered structural feature of Co/CZIF-12 can facilitate the Li$^+$ convenient diffusion during

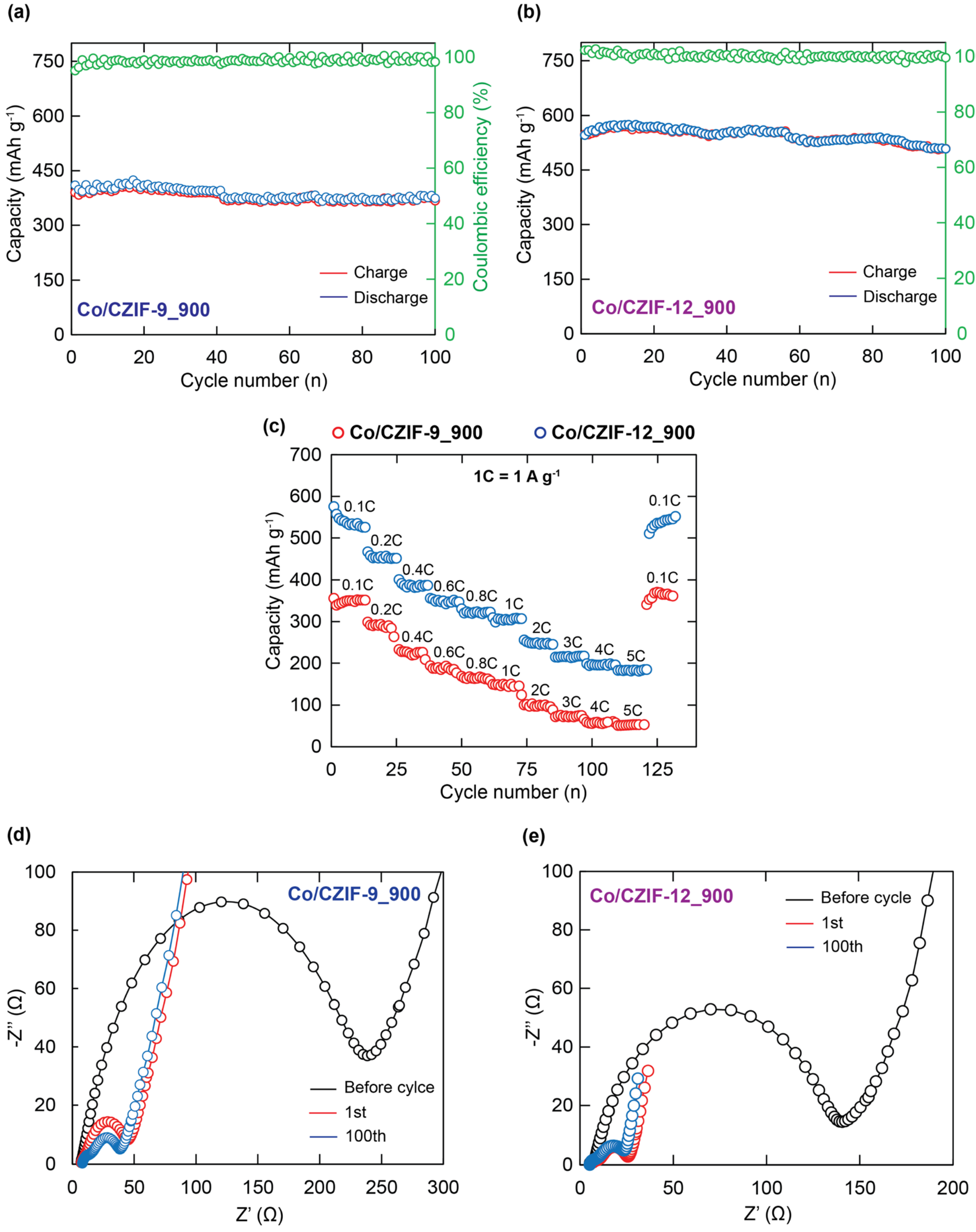

Fig. 8 The long-term cycling properties of Co/CZIF-9_900 (a) and Co/CZIF-12_900 (b) at 0.1 A g^{-1}; the rate performance of Co/CZIF-9_900 and Co/CZIF-12_900 at 0.1C to 5C (c) [1C = 1 A g^{-1}]; the Nyquist plots of Co/CZIF-9_900 (d) and Co/CZIF-12_900 (e).

the insertion/extraction of the Li$^+$ ion, increasing the storage capacity.[59,60]

The rate capability is considered an essential factor in evaluating the operating ability of energy storage devices in practical conditions. As given in Fig. 8c, the rate performances of the Co/CZIF-9_900 and Co/CZIF-12_900 composites are interpreted by the various current densities. Accordingly, Co/CZIF-12_900 displays the best rate capability under each current density compared to Co/CZIF-9_900. For Co/CZIF-12_900, the average specific charge capacities are 535.1, 452.4, 384.7, 368.5, 323.6, 303.8, 245.3, 213.2, 195.6, and 183.3 mA h g^{-1} at 0.1, 0.2, 0.4, 0.6, 0.8, 1.0, 2.0, 3.0, 4.0, and 5.0 A g^{-1}. There is obvious that the specific capacities decline with the rise of current density, which is elucidated in the mentioned rate tests. As the current density is back to 0.1 A g^{-1}, the specific charge capacity is restored to 551.8 mA h g^{-1}, implying an outstanding rate capability and reversibility. Similarly, the rate performances of the Co/CZIF-9 and Co/CZIF-12 calcined at 700 and 800 °C are

Table 1 The comparison of the Li^+ storage capacities at a current density of 0.1 A g^{-1} for Co/CZIF-9_900 and Co/CZIF-12_900 with the other porous carbon materials

Materials	Specific capacity at 0.1 A g^{-1}	Cycling stability at 0.1 A g^{-1}	Ref.
Co/CZIF-12_900	971.0 mA h g^{-1} at first discharge cycle 547.2 mA h g^{-1} after 3 cycles	508.8 mA h g^{-1} after 100 cycles	This work
Co/CZIF-9_900	883.1 mA h g^{-1} at first discharge cycle 383.2 mA h g^{-1} after 3 cycles	367.5 mA h g^{-1} after 100 cycles	This work
COF-derived porous carbon	505.7 mA h g^{-1} after 5 cycles	488.0 mA h g^{-1} after 100 cycles	62
B-doped porous carbon	697.0 mA h g^{-1} after 10 cycles	496.0 mA h g^{-1} after 100 cycles	63
Spheroidal carbon particles	290.0 mA h g^{-1} after 2 cycles	350.0 mA h g^{-1} after 200 cycles	64
N-doping hard carbon nanoshells	395.0 mA h g^{-1} after 15 cycles	245.0 mA h g^{-1} after 300 cycles at 1.5 A g^{-1}	65
HC-900	490.6 mA h g^{-1} after 1 cycle	125.3 mA h g^{-1} after 100 cycles	66
Bi@C composite	423.0 mA h g^{-1} after 1 cycle	300.0 mA h g^{-1} after 100 cycles	67
Se/CZIF-5	820.0 mA h g^{-1} at first discharge cycle	466.0 mA h g^{-1} after 80 cycles	68
CNF 800	798.0 mA h g^{-1} at first discharge cycle	300–400 mA h g^{-1} after 500 cycles at 0.5 A g^{-1}	69
PAC-KOH	775.0 mA h g^{-1} after 2 cycle	383.0 mA h g^{-1} after 150 cycles	70
NDPC	500.0 mA h g^{-1} after 50 cycles at 0.372 A g^{-1}	412.0 mA h g^{-1} after 200 cycles at 1.86 A g^{-1}	71
Porous C/Fe_3O_4	780.0 mA h g^{-1} at first discharge cycle	400.0 mA h g^{-1} after 200 cycles at 0.5 A g^{-1}	72

indicated in Section S5.† The fact shows that the Li^+ higher storage capacities for Co/CZIF-9 and Co/CZIF-12 annealed at 900 °C in comparison with the composites calcined at lower temperatures can be accounted for the incorporated effect between the nitrogen-doped carbon components and the Co nanoparticles, which could enhance the electrical conductivity, the structural stability of the carbon matrix, and restrict the volume expansion.[43,61]

To further confirm the electrical conductivity and the charge transfer property, the EIS analyses of Co/CZIF-9_900 and Co/CZIF-12_900 were performed in the frequency range of 10^6-10^{-2} Hz. Fig. 8d and e indicate the Nyquist plots of Co/CZIF-9_900 and Co/CZIF-12_900 electrodes with the samples before cycling, the first, and 100th cycle. Generally, the Nyquist plots of the composites can be observed through two main parts, including a sloping straight line at the low-frequency range and a depressed semicircle at the high-frequency range. Herein, the sloping straight line corresponds to the Warburg diffusion element (W_1) of the Li^+ diffusion process. In contrast, the semicircle one symbolizes the constant phase element (CPE_1) and the resistance of charge transfer (R_1) of the electrolyte/electrode interface, the resistance (R_2) and the constant phase element (CPE_2) of the SEI layer, and the internal resistance (R_3) of the cell (Fig. S11†). Based on the equivalent circuit combined with the Nyquist diagrams, the charge transfer resistance of Co/CZIF-9_900 and Co/CZIF-12_900 composites are 38.5 and 25.9 Ω after the first cycle, respectively. In addition, the Nyquist plots of Co/CZIF-9_900 and Co/CZIF-12_900 before and after the 100th cycle were analyzed. As a consequence, the semicircle diameters after the 100th cycle for Co/CZIF-9_900 and Co/CZIF-12_900 are 35.4 and 22.1 Ω, respectively. These values exhibit a decrease as compared to the samples before cycling. Interestingly, the resistance of charge transfer of Co/CZIF-12_900 reaches the smallest value with the low charge transfer impedance and contact, which contributes to the improvement of ionic diffusion and electrical conductivity during the discharge/charge process.

Notably, the difference in the specific discharge/charge capacity and cycling stability of the Co/CZIF-9 and Co/CZIF-12 annealed at the various temperatures with the previously reported porous carbon materials is illustrated in Table 1. It is noted that Co/CZIF-12_900 composite performs a higher specific capacity and cycling robustness after 100 cycles at a current density of 0.1 A g^{-1} as compared with the other anode electrodes. Hence, the Co/CZIF-12_900 material derived from the ZIF-12 structure with an RHO topology calcined at 900 °C can be considered an effective anode electrode material for LIBs.

4. Conclusion

In summary, we have successfully fabricated the Co/N-doped nanoporous carbon generation derived from the ZIF-9 and ZIF-12 precursors with different topologies for excellent electrochemical performance in LIBs. Remarkably, Co/CZIF-12_900 electrode indicates an outstanding electrochemical property compared to the remaining composites. Accordingly, the Co/CZIF-12_900 composite reaches a high reversible capacity of 547.2 mA h g^{-1} after the first 3 cycles and 508.8 mA h g^{-1} after 100 cycles at 0.1 A g^{-1} with an excellent rate capability. These high values can be explained by the fact that the Co/CZIF-12_900 material possesses a layered structure, high specific surface area, and rich mesopores, improving the Li^+ diffusion and storage. Furthermore, the presence of the Co nanoparticles and N-doping moieties in the carbon matrix can enhance the structural robustness and electrical conductivity and constrain the volume expansion of the material during the discharge/charge process. The obtained results demonstrate that the Co/CZIF-12_900 electrode is trusted to open up new synthetic investigations of the Co/N-doped porous carbon composites derived from the various ZIF backbones for energy storage devices with high performance.

Author contributions

M. V. N. formulated this project. M. V. N., A. T. A. D., H. V. N., M. V. T., Q. N. N., L. C. L., T. L. H. D., H. N. N.

synthesized the compounds and collected isotherms, powder X-ray diffraction patterns, FT-IR spectra, Raman spectra, TGA-DSC analysis. M. V. N. wrote the paper and all authors contributed to revising it. All authors have given approval to the final version of the manuscript.

Conflicts of interest

The authors maintain that they have no conflict of interest for this communication.

Acknowledgements

This work was supported by Ho Chi Minh City University of Education, Ho Chi Minh City, Vietnam, through Grant No. CS.2022.19.37.

Notes and references

1 Z. Yang, J. Zhang, M. C. Kintner-Meyer, X. Lu, D. Choi, J. P. Lemmon and J. Liu, Electrochemical energy storage for green grid, *Chem. Rev.*, 2011, **111**, 3577–3613.

2 J. B. Goodenough, Energy storage materials: A perspective, *Energy Storage Mater.*, 2015, **1**, 158–161.

3 L. Miao, J. Zhang, Y. Lv, L. Gan and M. Liu, Dendrite-free engineering toward efficient zinc storage: recent progress and future perspectives, *Chem. – Eur. J.*, 2023, **29**, e202203973.

4 L. Miao, Z. Song, W. Du, X. Zheng, Y. Lv, L. Gan and M. Liu, Advances in organic cathode materials for aqueous multivalent metal-ion storage, *Mater. Chem. Front.*, 2023, DOI: 10.1039/D3QM00297G.

5 B. Scrosati, J. Hassoun and Y. K. Sun, Lithium-ion batteries: a look into the future, *Energy Environ. Sci.*, 2011, **4**, 3287–3295.

6 L. Ji, Z. Lin, M. Alcoutlabi and X. Zhang, Recent developments in nanostructured anode materials for rechargeable lithium-ion batteries, *Energy Environ. Sci.*, 2011, **4**, 2682–2699.

7 J. B. Goodenough and K. S. Park, The Li-Ion Rechargeable Battery: A Perspective, *J. Am. Chem. Soc.*, 2013, **135**, 1167–1176.

8 S. S. Zhang, Problem, status, and possible solutions for lithium metal anode of rechargeable batteries, *ACS Appl. Energy Mater.*, 2018, **1**, 910–920.

9 Z. Zheng, H. H. Wu, H. Liu, Q. Zhang, X. He, S. Yu, V. Petrova, J. Feng, R. Kostecki, P. Liu, D. L. Peng, M. Liu and M. S. Wang, Achieving fast and durable lithium storage through amorphous FeP nanoparticles encapsulated in ultrathin 3D pdoped porous carbon nanosheets, *ACS Nano*, 2020, **14**, 9545–9561.

10 T. Wei, Z.-H. Zhang, Z.-M. Wang, Q. Zhang, Y.-S. Ye, J.-H. Lu, Zu. Rahman and Z.-W. Zhang, An ultra-thin solid composite electrolyte based on $Li_{6.4}La_3Zr_{1.4}Ta_{0.6}O_{12}$/PVDF-HFP/LiTFSI/succinonitrile for high-performance solid-state lithium metal battery, *ACS Appl. Energy Mater.*, 2020, **3**, 9428–9435.

11 X. Y. Yu and X. W. Lou, Mixed metal sulfides for electrochemical energy storage and conversion, *Adv. Energy Mater.*, 2018, **8**, 1701592.

12 A. D. Roberts, X. Li and H. Zhang, Porous carbon spheres and monoliths: morphology control, pore size tuning and their applications as li-ion battery anode materials, *Chem. Soc. Rev.*, 2014, **43**, 4341–4356.

13 J. Liao, R. Tan, Z. Kuang, C. Cui, Z. Wei, X. Deng, Z. Yan, Y. Feng, F. Li, C. Wang and J. Ma, Controlling the morphology, size and phase of Nb_2O_5 crystals for high electrochemical performance, *Chin. Chem. Lett.*, 2018, **29**, 1785–1790.

14 V. Etacheri, C. Wang, M. J. O'Connell, C. K. Chan and V. G. Pol, Porous carbon sphere anodes for enhanced lithium-ion storage, *J. Mater. Chem. A*, 2015, **3**, 9861–9868.

15 K. Zhou, S. Wang, S. Zhang, F. Kang and B. Li, Investigating the increased-capacity mechanism of porous carbon materials in lithium-ion batteries, *J. Mater. Chem. A*, 2020, **8**, 14031–14042.

16 K. Yu, Y. Wang, X. Wang, W. Liu, J. Liang and C. Liang, Preparation of porous carbon anode materials for lithium-ion battery from rice husk, *Mater. Lett.*, 2019, **253**, 405–408.

17 B. Y. Guan, X. Y. Yu, H. B. Wu and X. W. Lou, Complex nanostructures from materials based on metalorganic frameworks for electrochemical energy storage and conversion, *Adv. Mater.*, 2017, **29**, 1703614.

18 Y. Mao, H. Duan, B. Xu, L. Zhang, Y. Hu, C. Zhao, Z. Wang, L. Chen and Y. Yang, Lithium storage in nitrogen-rich mesoporous carbon materials, *Energy Environ. Sci.*, 2012, **5**, 7950.

19 H. C. Zhou, J. R. Long and O. M. Yaghi, Introduction to metal-organic frameworks, *Chem. Rev.*, 2012, **112**, 673–674.

20 H. Furukawa, K. E. Cordova, M. O'Keeffe and O. M. Yaghi, The chemistry and applications of metal–organic frameworks, *Science*, 2013, **341**, 1230444–1230456.

21 H. C. Zhou and S. Kitagawa, Metal–organic frameworks (MOFs), *Chem. Soc. Rev.*, 2014, **43**, 5415–5418.

22 B. Li, Y. Zhang, R. Krishna, K. Yao, Y. Han, Z. Wu, D. Ma, Z. Shi, T. Pham, B. Space, J. Liu, P. K. Thallapally, J. Liu, M. Chrzanowski and S. Ma, Introduction of π-complexation into porous aromatic framework for highly selective adsorption of ethylene over ethane, *J. Am. Chem. Soc.*, 2014, **136**, 8654–8660.

23 T. T. M. Bui, L. T. Nguyen, N. P. H. Pham, C. C. Tran, L. T. Nguyen, T. A. Nguyen, H. N. Nguyen and M. V. Nguyen, A new approach for ultra-high adsorption of cationic methylene blue in a Zr-sulfonic-based metal–organic framework, *RSC Adv.*, 2021, **11**, 36626–36635.

24 B. Valizadeh, T. N. Nguyen, S. Kampouri, D. T. Sun, M. D. Mensi, K. Stylianou, B. Smit and W. L. Queen, A novel integrated Cr(VI) adsorption-photoreduction system using MOF@polymer composite beads, *J. Mater. Chem. A*, 2020, **8**, 9629–9637.

25 R. M. Rego, G. Sriram, K. V. Ajeya, H. Y. Jung, M. D. Kurkuri and M. Kigga, Cerium based UiO-66 MOF as a multipollutant adsorbent for universal water purification, *J. Hazard. Mater.*, 2021, **416**, 125941.

26 C. C. Tran, H. C. Dong, V. T. N. Truong, T. T. M. Bui, H. N. Nguyen, T. A. T. Nguyen, N. N. Dang and M. V. Nguyen, Enhancing the remarkable adsorption of Pb^{2+} in a series of sulfonic-functionalized Zr-based MOFs: a combined theoretical and experimental study for elucidating the adsorption mechanism, *Dalton Trans.*, 2022, **51**, 7503–7516.

27 Y. B. Huang, J. Liang, X. S. Wang and R. Cao, Multifunctional metal–organic framework catalysts: synergistic catalysis and tandem reactions, *Chem. Soc. Rev.*, 2017, **46**, 126–157.

28 T. Toyao, M. Saito, Y. Horiuchi, K. Mochizuki, M. Iwata, H. Higashimura and M. Matsuoka, Efficient hydrogen production and photocatalytic reduction of nitrobenzene over a visible-light-responsive metal–organic framework photocatalyst, *Catal. Sci. Technol.*, 2013, **3**, 2092–2097.

29 L. Yang, C. Lian, X. Li, Y. Han, L. Yang, T. Cai and C. Shao, Highly selective bifunctional luminescent sensor toward nitrobenzene and Cu^{2+} ion based on microporous metal–organic frameworks: synthesis, structures, and properties, *ACS Appl. Mater. Interfaces*, 2017, **9**, 17208–17217.

30 L. E. Kreno, K. Leong, O. K. Farha, M. Allendorf, R. P. V. Duyne and J. T. Hupp, Metal-organic framework materials as chemical sensors, *Chem. Rev.*, 2012, **112**, 1105–1125.

31 X. Meng, H. N. Wang, S. Y. Song and H. J. Zhang, Proton conducting crystalline porous materials, *Chem. Soc. Rev.*, 2017, **46**, 464–480.

32 K. M. L. Taylor, A. Jin and W. Lin, Surfactant-assisted synthesis of nanoscale gadolinium metal–organic frameworks for potential multimodal imaging, *Angew. Chem., Int. Ed. Engl.*, 2008, **47**, 7722–7725.

33 D. Liu, R. C. Huxford and W. Lin, Phosphorescent nanoscale coordination polymers as contrast agents for optical imaging, *Angew. Chem., Int. Ed. Engl.*, 2011, **50**, 3696–3700.

34 Z. Li, L. Y. Zhang, L. Zhang, J. Huang and H. Liu, ZIF-67-Derived CoSe/NC composites as anode materials for lithium-ion batteries, *Nanoscale Res. Lett.*, 2019, **14**, 358.

35 Y. Chang, C. Huang and W. Liu, Co/ZnO/nitrogen-doped carbon composite anode derived from metal organic frameworks for lithium ion batteries, *Polymers*, 2022, **14**, 3085.

36 F. Zheng, Y. Yang and Q. Chen, High lithium anodic performance of highly nitrogen-doped porous carbon prepared from a metal-organic framework, *Nat. Commun.*, 2014, **5**, 5261.

37 Y. M. Chen, L. Yu and X. W. Lou, Hierarchical tubular structures composed of Co_3O_4 hollow nanoparticles and carbon nanotubes for lithium storage, *Angew. Chem., Int. Ed.*, 2016, **55**, 5990–5993.

38 M. He, J. Yao, Q. Liu, Z. Zhong and H. Wang, Toluene-assisted synthesis of RHO-type zeolitic imidazolate frameworks: synthesis and formation mechanism of ZIF-11 and ZIF-12, *Dalton Trans.*, 2013, **42**, 16608–16613.

39 G. Khandelwal, N. P. M. J. Raj and S. Kim, Zeolitic imidazole framework: metal–organic framework subfamily members for triboelectric nanogenerators, *Adv. Funct. Mater.*, 2020, **30**, 1910162.

40 K. S. Park, Z. Ni, A. P. Cote, J. Y. Choi, R. Huang, F. J. Uribe-Romo, H. K. Chae, M. O'Keeffe and O. M. Yaghi, Exceptional chemical and thermal stability of zeolitic imidazolate frameworks, *Proc. Natl. Acad. Sci. U. S. A.*, 2006, **103**, 10186–10191.

41 A. Noguera-Díaz, J. Villarroel-Rocha, V. P. Ting, N. Bimbo, K. Sapag and T. J. Mays, Flexible ZIFs: probing guest-induced flexibility with CO_2, N_2 and Ar adsorption, *J. Chem. Technol. Biotechnol.*, 2019, **94**, 3787–3792.

42 L. Zhu, L. Xie and X. Cao, LiV_3O_8/polydiphenylamine composites with significantly improved electrochemical behavior as cathode materials for rechargeable lithium batteries, *Chem. Eng. J.*, 2018, **351**, 169–176.

43 L. Wang, Z. Wang, L. Xie, L. Zhu and X. Cao, ZIF-67-derived N-doped Co/C nanocubes as high performance anode materials for lithium-ion batteries, *ACS Appl. Mater. Interfaces*, 2019, **11**, 16619–16628.

44 A. C. Ferrari and D. M. Basko, Raman spectroscopy as a versatile tool for studying the properties of graphene, *Nat. Nanotechnol.*, 2013, **8**, 235–246.

45 G. Ćiric-Marjanovic, I. Pasti, N. Gavrilov, A. Janosevic and S. Mentus, Carbonised polyaniline and polypyrrole: towards advanced nitrogen-containing carbon materials, *Chem. Pap.*, 2013, **67**, 781–813.

46 Y. Guo, J. Tang, R. R. Salunkhe, Z. A. Alothman, M. S. A. Hossain, V. Malgras and Y. Yamauchi, Effect of various carbonization temperatures on zif-67 derived nanoporous carbons, *Bull. Chem. Soc. Jpn.*, 2017, **90**, 939–942.

47 X. Wang and Y. Li, Nanoporous carbons derived from MOFs as metal-free catalysts for selective aerobic oxidations, *J. Mater. Chem. A*, 2016, **4**, 5247–5257.

48 L. Chen, X. Zhang, H. Liang, M. Kong, Q. Guan, P. Chen, Z. Wu and S. Yu, Synthesis of nitrogen-doped porous carbon nanofibers as an efficient electrode material for supercapacitors, *ACS Nano*, 2012, **6**, 7092–7102.

49 M. C. Biesinger, B. P. Payne, A. P. Grosvenor, L. W. M. Lau, A. R. Gerson and R. S. C. Smart, Resolving surface chemical states in XPS analysis of first row transition metals, oxides and hydroxides: Cr, Mn, Fe, Co and Ni, *Appl. Surf. Sci.*, 2011, **257**, 2717–2730.

50 J. Li, D. Yan, T. Lu, Y. Yao and L. Pan, An advanced CoSe embedded within porous carbon polyhedra hybrid for high performance lithium-ion and sodium-ion batteries, *Chem. Eng. J.*, 2017, **325**, 14–24.

51 F. Wang, H. Y. Zhuo, X. G. Han, W. Chen and D. Sun, Foam-like CoO@N,S-codoped carbon composites derived from a well-designed N,S-rich Co-MOF for lithium-ion batteries, *J. Mater. Chem. A*, 2017, **5**, 22964–22969.

52 Y. Zhou, R. Tian, H. Duan, K. Wang, Y. Guo, H. Li and H. Liu, CoSe/Co nanoparticles wrapped by in situ grown N-doped graphitic carbon nanosheets as anode material for advanced lithium ion batteries, *J. Power Sources*, 2018, **399**, 223–230.

53 H. Hu, J. Zhang, B. Guan and X. W. Lou, Unusual formation of CoSe@carbon nanoboxes, which have an inhomogeneous

shell, for efficient lithium storage, *Angew. Chem., Int. Ed.*, 2016, **55**, 9514–9518.

54 K. Xu, Y. Li, J. Xiong, X. Ou, W. Su, G. Zhong and C. Yang, Porosity derived from camellia pollen grains as anode materials for lithium/sodium ion batteries, *Front. Chem.*, 2018, **6**, 366.

55 A. Li, Y. Tong, B. Cao, H. Song, Z. Li, X. Chen, J. Zhou, G. Chen and H. Luo, MOF-derived multifractal porous carbon with ultrahigh lithium-ion storage performance, *Sci. Rep.*, 2017, **7**, 1–8.

56 J. Yue, X. Zhao and D. Xia, Electrochemical lithium storage of C/Co composite as an anode material for lithium ion batteries, *Electrochem. Commun.*, 2012, **18**, 44–47.

57 M. Deng, S. Li, W. Hong, Y. Jiang, W. Xu, H. Shuai, G. Zou, Y. Hu, H. Hou, W. Wang and X. Ji, Octahedral Sb_2O_3 as highperformance anode for lithium and sodium storage, *Mater. Chem. Phys.*, 2019, **223**, 46–52.

58 W. Liu, Y. Fu, Y. Li, S. Chen, Y. Song and L. Wang, Three dimensional carbon foam surrounded by carbon nanotubes and Co-Co_3O_4 nanoparticles for stable lithium-ion batteries, *Composites, Part B*, 2019, **163**, 464–470.

59 L. Guo, L. Cao, J. He, J. Huang, J. Li, K. Kajiyoshia and S. Chen, Layered-structure $(NH_4)_2Mo_4O_{13}$@N-doped porous carbon composite as a superior anode for lithium-ion batteries, *Chem. Commun.*, 2020, **56**, 7757–7760.

60 A. Chakraborty, S. Kunnikuruvan, S. Kumar, B. Markovsky, D. Aurbach, M. Dixit and D. T. Major, Layered cathode materials for lithium-ion batteries: review of computational studies on $LiNi_{1-x-y}Co_xMn_yO_2$ and $LiNi_{1-x-y}Co_xAl_yO_2$, *Chem. Mater.*, 2020, **32**, 915–952.

61 D. Wang, B. Yan, Y. Guo, L. Chen, F. Yu and G. Wang, N-doped carbon coated CoO nanowire arrays derived from zeolitic imidazolate framework-67 as binder-free anodes for high-performance lithium storage, *Sci. Rep.*, 2019, **9**, 5934.

62 X. J. Zhang, G. Zhu, M. Wang, J. B. Li, T. Lu and L. K. Pan, Covalent-organic-frameworks derived N-doped porous carbon materials as anode for superior long-life cycling lithium and sodium ion batteries, *Carbon*, 2017, **116**, 686–694.

63 D. Wang, Z. Wang, Y. Li, K. Dong, J. Shao, S. Luo, Y. Liu and X. Qi, In situ double-template fabrication of boron-doped 3D hierarchical porous carbon network as anode materials for Li- and Na-ion batteries, *Appl. Surf. Sci.*, 2019, **464**, 422–428.

64 K. Kim, R. A. Adams, P. J. Kim, A. Arora, E. Martinez, J. P. Youngblood and V. G. Pol, Li-ion storage in an amorphous, solid, spheroidal carbon anode produced by dry-autoclaving of coffee oil, *Carbon*, 2018, **133**, 62–68.

65 F. Zhao, X. Zhao, B. Peng, F. Gan, M. Yao, W. Tan, J. Dong and Q. Zhang, Polyimide-derived carbon nanofiber membranes as anodes for high-performance flexible lithium ion batteries, *Chin. Chem. Lett.*, 2018, **29**, 1692–1697.

66 Y. Wang, Y. Li, S. S. Mao, D. Ye, W. Liu, R. Guo, Z. Feng, J. Kong and J. Xie, N-doped porous hard-carbon derived from recycled separators for efficient lithium-ion and sodium-ion batteries, *Sustainable Energy Fuels*, 2019, **3**, 717–722.

67 C. M. Park, S. Yoon, S. I. Lee and H. J. Sohn, Enhanced electrochemical properties of nanostructured bismuth-based composites for rechargeable lithium batteries, *J. Power Sources*, 2009, **186**, 206–210.

68 M. H. A. Shiraz, E. Rehl, H. Kazemian and J. Liu, Durable lithium/selenium batteries enabled by the integration of MOF-derived porous carbon and alucone coating, *Nanomaterials*, 2021, **11**, 1976.

69 M. Nazhipkyzy, A. B. Maltay, K. Askaruly, D. D. Assylkhanova, A. R. Seitkazinova and Z. A. Mansurov, Biomass-derived porous carbon materials for Li-Ion battery, *Nanomaterials*, 2022, **12**, 3710.

70 R. Boonprachai, T. Autthawong, O. Namsar, C. Yodbunork, W. Yodying and T. Sarakonsri, Natural porous carbon derived from popped rice as anode materials for lithium-ion batteries, *Crystals*, 2022, **12**, 223.

71 H. Sun, M. Xiao and F. Zhu, Nitrogen doped porous carbon with high rate performance for lithium ion storage, *J. Electroanal. Chem.*, 2023, **932**, 117254.

72 A. Adi and I. Taniguchi, Synthesis of porous C/Fe_3O_4 microspheres by spray pyrolysis with $NaNO_3$ additive for lithium-ion battery applications, *J. Solid State Electrochem.*, 2023, **307**, 1–11.